

Effect of Heat-Treatment Schedule on the Microstructure and Mechanical Properties of Cold-Rolled Dual-Phase Steels

Yong-Gang Deng¹ · Hong-Shuang Di¹ · Jie-Cen Zhang¹

Received: 20 April 2015/Revised: 30 June 2015/Published online: 15 August 2015
© The Chinese Society for Metals and Springer-Verlag Berlin Heidelberg 2015

Abstract Low-carbon (0.08 wt% C) steel has been subjected to three different heat treatments to obtain dual-phase steels with different microstructures. An understanding of structure–property was established through tensile tests, in conjunction with scanning electron microscope and transmission electron microscope. The results show that the steel after intermediate quenching (IQ) consisting of fine and fibrous martensite exhibited the intermediate strength, highest elongation and the best comprehensive performance of mechanical properties, whereas the steel subjected to intercritical annealing (IA) produced a network martensite along ferrite grain boundaries, having the lowest strength and intermediate elongation. Besides, step quenching (SQ) resulted in a coarse and blocky ferrite–martensite microstructure showing the worst mechanical properties of the three different heat-treatment conditions. The strain-hardening behavior was studied through the modified Crussard–Jaoul model, indicating two stages of strain-hardening behavior for all three samples. The highest magnitude of strain-hardening ability was obtained by IQ annealing routes. The analysis of the fractured surface revealed that ferrite/martensite interfaces are the most susceptible for microvoid nucleation. However, martensite microcracks were also observed in SQ sample, and the microvoids are nucleated within the ferrite grain in IA sample as well. The variations in strength, elongation, strain-hardening behavior and fracture mechanism of the steel with different heat-treatment schedules were further discussed in relation to the microstructural features.

KEY WORDS: Dual-phase steel; Heat-treatment schedule; Strain-hardening behavior; Fracture mechanism

1 Introduction

With the development of the modern automobile industry, the application of lightweight components is a challenge. Due to the economic and ecological considerations, the reduction in mass is desired. Dual-phase (DP) steel is low-carbon and low-alloy steel with (10–30) vol% of martensite and a ductile ferrite matrix, which is widely used in the automotive

industry because of the good combination of high strength and good formability at low production costs [1–4].

DP steel is characterized by a continuous yielding behavior with a low initial flow stress and a high initial strain-hardening rate [5–8]. These properties provide the advantages over the conventional high-strength low-alloy steels, while at the same time it also introduces some certain risk factors [9], including strong stress/strain partitioning [10, 11], strain localization [12, 13] and damage evolution [14].

The mechanical properties of the dual-phase steels are determined by the shape, the size and the volume fraction of the constituent phases. These, in turn, are dependent on the annealing parameters and alloying elements. So far, some researchers have studied about the effect of the martensite on the properties of ferrite–martensite dual-phase steels,

Available online at <http://link.springer.com/journal/40195>

✉ Hong-Shuang Di
dhshuang@mail.neu.edu.cn

¹ State Key Laboratory of Rolling and Automation, Northeastern University, Shenyang 110819, China

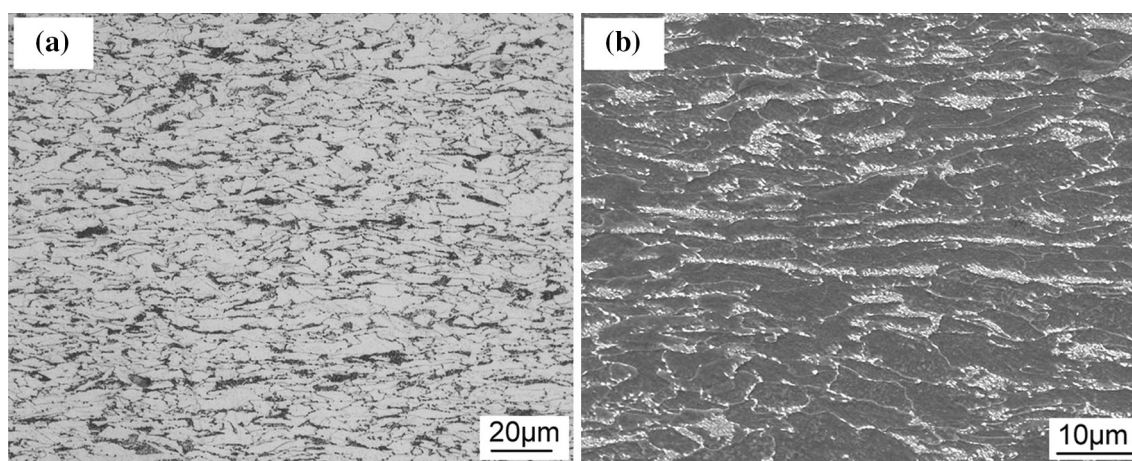


Fig. 1 Microstructure of the as-received cold-rolled steel: **a** OM, **b** SEM

including the content [15, 16], martensite morphology, distribution martensite and the grain size [17–24].

The tensile properties of DP steels have been investigated widely. Many studies have presented an increase in the tensile strength with increasing martensite volume fraction (V_m) of DP steels [15, 16, 25]. Maleque *et al.* [16] reported that the increase in the tensile strength could be obtained through the increase in the V_m . Bag *et al.* [15] found that the optimal properties were achieved at $\sim 0.55 V_m$. A further increase in V_m was found to decrease the tensile strength.

Das *et al.* [17] obtained different microstructures with similar V_m and found that a fine fibrous structure had a beneficial effect on the mechanical properties. In references [26, 27], the strain-hardening behavior, fracture mechanism and microvoid formation were correlated to the martensite morphology and distribution. It was pointed out that the martensite morphology affected the strain-hardening and the fracture properties. Bhattacharyya *et al.* [28] developed a model to describe the effect of the martensite morphology on the initial plastic state of the ferrite matrix and the stress–strain behavior of DP steels during loading. In addition, Hüseyin [29] and Bayram [30] also investigated the effect of the grain size of constituents on the mechanical properties of DP steels. They found that fine microstructural constituents can provide the best combination of strength and ductility of DP steel due to the decrease in the stress/strain partitioning between ferrite and martensite. All the studies showed that the morphology of martensite had a significant impact on the mechanical properties of DP steels.

In case of conventional continuous annealing, the cold-rolled ferrite + pearlite subjected to the intercritical annealing produced a chain-like network or banded structure of the martensite, leading to the decrease in the ductility.

However, suitable heat-treatment procedures can produce excellent ferrite–martensite microstructure and thus the optimal comprehensive mechanical properties. In this study, ferrite–martensite microstructure with different martensite morphologies and contents were obtained through a careful design of the heat-treatment schedules. A comparison of the mechanical properties among all the samples reveals that the steel subjected to intermediate quenching (IQ) treatment may greatly improve the mechanical properties.

2 Experimental

2.1 Material

An industrial cold-rolled low-carbon steel sheet with an initial thickness of 1.5 mm was investigated in the present study. The chemical composition is Fe–0.08C–0.42Si–1.83Mn–0.16P–0.18Cr (wt%). Microstructure of the as-received state is shown in Fig. 1, which is composed of 15 vol% pearlite and 85 vol% ferrite.

2.2 Heat Treatment

The A_{c1} and A_{c3} temperatures can be calculated by the empirical equations in Ref. [16]:

$$A_{c1} = 723 - 10.7\text{Mn} - 16.9\text{Ni} + 29.1\text{Si} + 16.9\text{Cr} + 290\text{As} + 6.38\text{W}. \quad (1)$$

$$A_{c3} = 910 - 203\sqrt{C} - 15.2\text{Ni} + 44.7\text{Si} + 104\text{V} + 31.5\text{Mo} + 13.1\text{W}. \quad (2)$$

where the unit of A_{c1} and A_{c3} is $^{\circ}\text{C}$ and the unit of the equations is wt%. According to Eqs. (1) and (2), the A_{c1} and A_{c3} are 721 and 871 $^{\circ}\text{C}$, respectively.

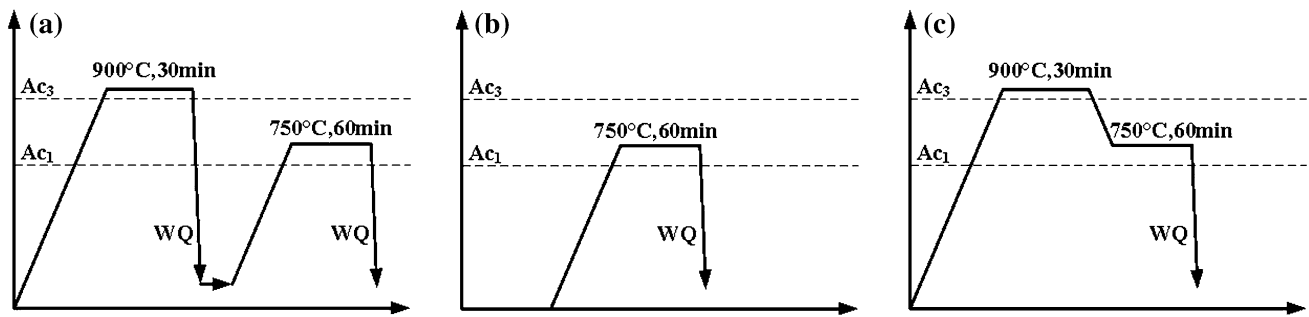


Fig. 2 Schematics of the three kinds of heat-treatment schedules studied: **a** IQ, **b** IA, **c** SQ. *WQ* means water quenching

In order to analyze the effect of the heat-treatment schedule on the microstructure and the tensile properties, the steel was subjected to three different processing schedules as illustrated in Fig. 2.

1. Intermediate quenching (IQ): The steel was first austenized at 900 °C for 30 min and water-quenched. Then, an intercritical annealing was conducted at 750 °C for 60 min followed by water quenching (Fig. 2a).
2. Intercritical annealing (IA): The intercritical annealing was directly applied to the initial cold-rolled ferrite + pearlite microstructure (Fig. 2b).
3. Step quenching (SQ): After the austenization at 900 °C for 30 min, the steel was cooled down to 750 °C at the rate of 1 °C/min and held for 60 min before the final water quenching (Fig. 2c).

2.3 Tensile Tests

According to ASTM A370-07a standard, the tensile samples are prepared with a nominal gauge length of 50 mm and width of 12.5 mm. The tensile tests were carried out at room temperature using a 100-kN Instron tensile machine at a crosshead speed of 2 mm/min.

2.4 Microstructure Characterization

Microstructure examination was performed with a Leica DM 2500-M metallographic microscope (OM) and Quanta FEM 250 scanning electron microscope (SEM). The transmission electron microscopy (TEM) analysis was conducted using FEI Tecnai G2F20S-TWIN microscope. Thin foils were electro-polished to perforation using a twin-jet electro-polished device with an electrolyte consisting of 4% perchloric acid and 96% ethanol. The volume fraction of the martensite and the grain size of the ferrite were obtained using the image-processing software, Image-Pro-Plus.

3 Results and Discussion

3.1 Microstructure Evolution

Figure 3 shows the SEM micrographs of the samples after the heat treatments, where ferrite–martensite DP microstructure can be clearly identified. However, the morphology, the size and distribution of the martensite phase are closely related to the heat-treatment schedules.

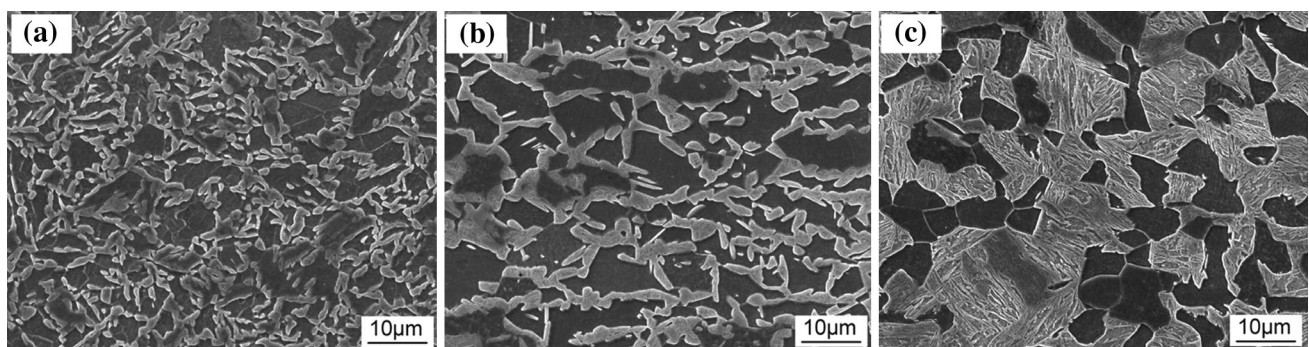


Fig. 3 SEM images of DP microstructure obtained by IQ **a**, IA **b**, SQ **c**

For the IQ specimen, the intercritical annealing was initiated from lath martensite substructure, which is able to provide sufficient nucleation sites for austenite formation [15], such as the prior austenite grain boundaries, the carbide precipitates on prior austenite grain boundaries, the spheroids in ferrite and the fine carbide arrays formed on the prior martensite plate/lath boundaries. Finally, the fine and fibrous morphologies of martensite were achieved.

In the case of IA treatment, pearlite colonies locate at the ferrite grain boundaries as shown in Fig. 1. As presented in [31–33], the austenite nucleates at the ferrite–pearlite interface and then grows into the ferrite after the fully dissolution of pearlite. Meanwhile, as a competitive event, the nucleation of the austenite at the recrystallized ferrite grain boundaries is also carried out and results in the formation of a network of austenite phase. After quenching from the intercritical temperature, a corresponding martensite network is obtained (Fig. 3b).

In contrast to the IQ and IA samples, a blocky morphology of the martensite was shown in the SQ sample (Fig. 3c). In this process, the sample was first completely austenitized, before entering into the $\alpha + \gamma$ region. Therefore, the ferrite grain would nucleate at the austenite grain boundaries and grow toward the austenite grain interior [33]. Meanwhile, austenite also grows at the same time, such a case yielded coarse block martensite grains.

Image analysis of the micrographs in Fig. 3 revealed the lowest amounts of the martensite in the IA sample (Table 1). This can be explained as follows. Starting from cold-rolled “ferrite + pearlite” microstructure, the heavily deformed ferrite grains would recrystallize upon heating to

the intercritical temperature. The nucleation of the austenite becomes unfavorable at moving ferrite boundaries [31], leading to the decreased volume fraction of the austenite and therefore less martensite after quenching. Compared with the IQ sample, austenite-to-ferrite transformation occurred during the intercritical annealing and the ferrite nucleated primarily at the austenite grain boundaries. The difference in nucleation density of produced phase between IQ and SQ samples plays an important role in determining the martensite volume fraction.

Figure 4 shows the TEM micrographs of the samples after different heat-treatment schedules. As can be seen from figures, high density of dislocation in the ferrite grains close to the interface was identified, which was a consequence of volume expansion associated with the austenite-to-martensite transformation. These dislocations are mobile and usually regarded as geometrically necessary dislocations, playing important roles in continuous yielding [34]. The absence of the bainite in the microstructure indicates the good hardenability of the steels.

3.2 Tensile Property

The engineering and true stress–strain curves are presented in Fig. 5. Continuous yielding with the yield ratio below 0.6 was observed in every sample, which is characteristic stress–strain behavior of dual-phase steels [35, 36].

Mechanical properties are summarized in Table 1. The SQ sample exhibits highest strength but lowest elongation, while the IA sample shows lowest strength and intermediate elongation. Optimal mechanical properties including

Table 1 Mechanical properties obtained from the tensile tests and microstructural characteristics obtained from SEM micrographs

Specimen	YS (MPa)	UTS (MPa)	TEL (%)	UE (%)	UTS \times UE (MPa%)	Yield ratio	d_f (μm)	V_m (%)
IQ	399.6	754.9	19.9	12.3	9285	0.53	7.3	45.7
IA	382.7	700.4	16.4	10.1	7074	0.55	10.2	36.2
SQ	488.3	838.7	13.8	7.5	6290	0.58	9.4	55.3

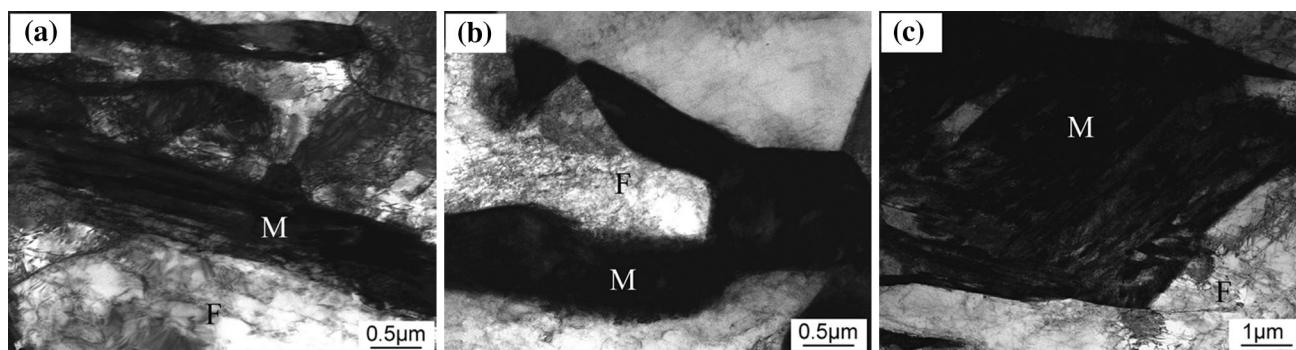


Fig. 4 TEM images of the annealed samples: a IQ, b IA, c SQ (*F* ferrite, *M* martensite)

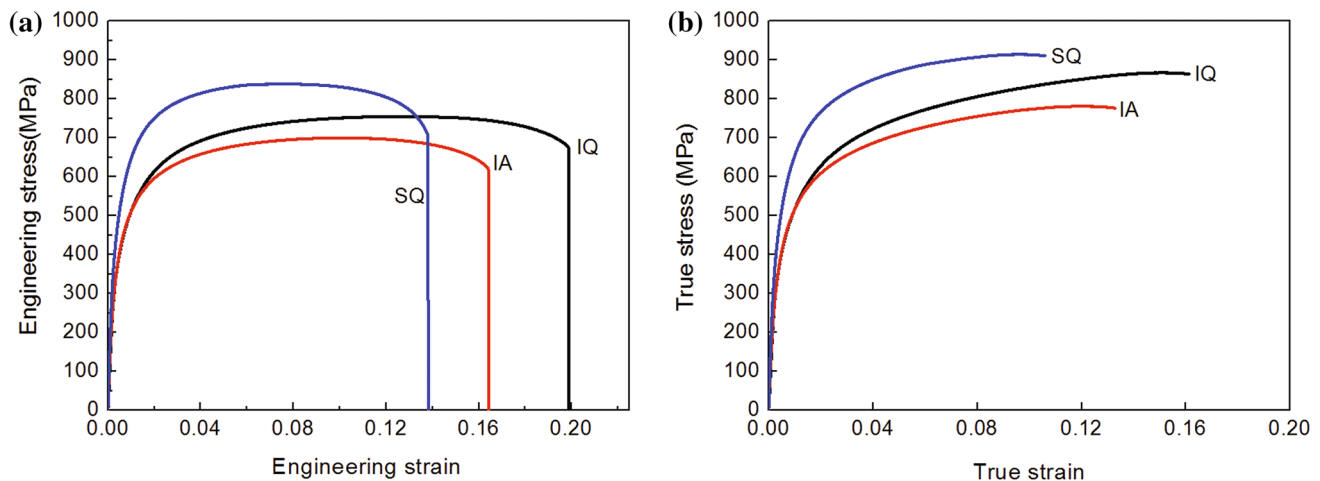


Fig. 5 Engineering **a**, true stress–strain **b** curves of the investigated steels

moderate strength and highest magnitude of ductility were achieved in the IQ treatment. The product of ultimate strength and uniform elongation ($UTS \times UE$) of the IQ sample (i.e., 92.9 J cm^{-3}) is superior when compared to that of other two samples (70.7 and 62.9 J cm^{-3} for IA and SQ samples, respectively).

Based on the rule of mixture, the difference in ultimate strength (UTS) can be related to the martensite volume fraction (V_m) (Table 1). The better elongation [total elongation (TEL) and uniform elongation (UE)] of the IQ sample compared to other two samples could be ascribed to the finer grain structure and the fibrous martensite uniformly distributed in the ferrite matrix. Calcagnotto *et al.* [20, 21] reported a more efficient load transfer between soft ferrite and hard martensite for a finer grain microstructure where higher fraction of ferrite–martensite interfaces is present. Thereafter, the lower stress concentration at ferrite–martensite interfaces led to more relaxation of strain and therefore the higher ductility. In addition, uniform distribution of the martensite also resulted in lower stress concentration and uniform strain distribution, delaying the plastic instability or necking of the material to higher strains.

3.3 Strain-Hardening Behavior

A study by Colla *et al.* [37] showed that modified C–J analysis based on Swift equation can describe the multi-stage strain-hardening behavior of dual-phase steel, which is based on the following equation:

$$\varepsilon = \varepsilon_0 + k\sigma^m. \quad (3)$$

Differentiating the previous equation with respect to ε and expressing in logarithmic form is:

$$\ln(d\sigma/d\varepsilon) = (1 - m) \ln \sigma - \ln(km). \quad (4)$$

where σ and ε are true stress and true strain, respectively, k is the constant which is normally called the strength coefficient, ε_0 is the maximum elastic strain and $(1 - m)$ is the slope. It can be seen that the strain-hardening ability decreases with increasing m . Corresponding to the stress–strain curves in Fig. 5, Fig. 6 shows the plots of $\ln(d\sigma/d\varepsilon)$ versus $\ln \sigma$. Using linear fitting, the $1/m$ was obtained and indicated in Fig. 6.

The plots of $\ln(d\sigma/d\varepsilon)$ versus $\ln \sigma$ clearly reveal two distinct stages of strain hardening, which is related to different deformation mechanisms. The first stage (stage I) with the lower slope, representing higher strain-hardening ability, is attributed to deformation of soft ferrite matrix alone assisted by mobile dislocations present near the martensite regions. The second stage (stage II) with the higher slope, corresponding to the lower strain-hardening ability, is attributed to uniform deformation of hard martensite and already strain-hardened ferrite. Two stages of strain hardening by modified C–J technique have been demonstrated earlier for DP steels [17, 38].

As indicated in Fig. 6, $1/m$ decreases in the order of $IQ > IA > SQ$, for either stage. Son *et al.* [39] and Mazaheri *et al.* [40] reported a 4% volume expansion from the martensitic transformation of the austenite, which led to the creation of geometrically necessary dislocations (GNDs) along the ferrite–martensite interfaces in the ferrite grains. Then, a higher strain-hardening rate would be expected from the higher fraction of ferrite–martensite interface. Besides, decreasing the size of martensite islands would be favorable for achieving higher strain-hardening rate in DP steels [41].

Furthermore, martensite morphology also affects the strain-hardening behavior in DP steels. According to Mazinani and Poole [42], the martensite plasticity is favored by changing the martensite island's morphology

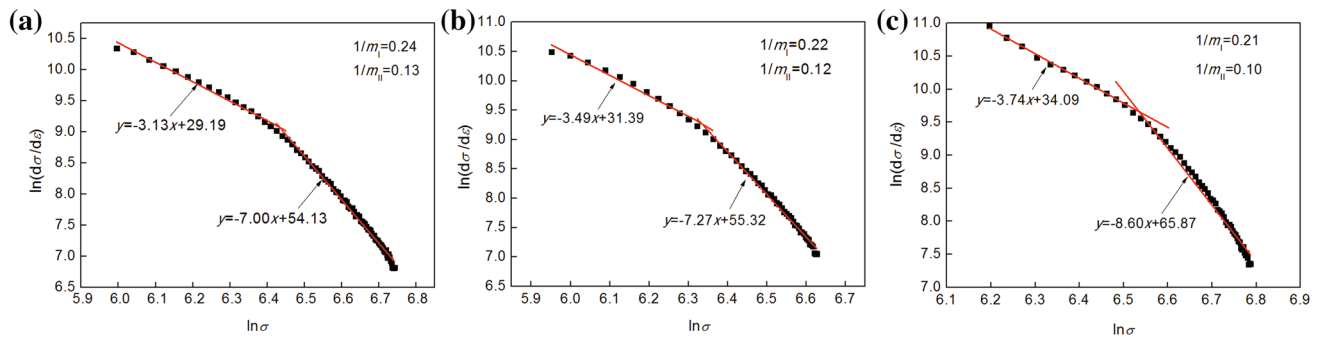


Fig. 6 Modified C–J plots of $\ln(d\sigma/d\varepsilon)$ versus $\ln \sigma$ for ferrite–martensite DP microstructures developed by varying heat-treatment paths: **a** IQ, **b** IA, **c** SQ

from equiaxed to band. In the present study, owing to the higher plastic deformation ability of coarse and nearly banded martensite particles (SQ sample), as compared to fine and equiaxed martensite particles (IQ and IA samples), the lower strain-hardening ability in the former rather than in the latter would be expected. Higher strain-hardening rate delays the onset of necking and therefore increases uniform elongation and total elongation (Table 1).

3.4 Fracture Mechanisms

Figure 7 shows the fractured surfaces of the heat-treated samples, where dimples are observed in the IQ and IA samples while cleavage fracture is also present in SQ sample. It is known that the ductile fracture in DP steels occurs in three sequential stages, i.e., void nucleation, void growth and void coalescence, which resulted in the dimpled fracture surface. Microvoids which nucleated at the ferrite–martensite interfaces usually grow within the more ductile ferrite matrix. The difference in fracture mechanism could be attributed to the morphology and distribution of the martensite. For the banded and interconnected martensite islands, compared to the fine and isolated martensite islands, more cleavage facets would be generated [7, 42]. The interconnected martensite, which located

along the ferrite grain boundaries, cracked easily and predominantly resulted in the cleavage fracture mode. However, martensite cracking was less frequent and the microvoids were smaller and microvoid density was higher in the specimen with fine martensite particles, and the fracture formed was a dimple depression type.

To further elucidate the effect of the microstructures on ductility, the cross-sectional area beneath the fractured surfaces was also analyzed as shown in Fig. 8.

Higher density of voids appeared in the IQ and IA samples (Fig. 8a, b) is noticeable, which have higher true strains at fracture. In contrast, the microstructural damage in the form of voids is considerably less in the SQ sample (Fig. 8c) with a much lower fracture strain. These observations are consistent with the earlier report [43]. In addition, the fracture surface for IQ and IA samples exhibited a vivid jagged edge as marked by red arrow in Fig. 8, which stands for a longer path for void coalescence and therefore a higher elongation before fracture.

In order to reveal the preferred void nucleation sites, the cross-sectional area beneath the fracture surface was further analyzed by SEM. As can be seen from Fig. 9, the frequent nucleation of the microvoids at the ferrite/martensite interfaces irrespective of the heat-treatment schedules (as marked by the black arrow) can be observed.

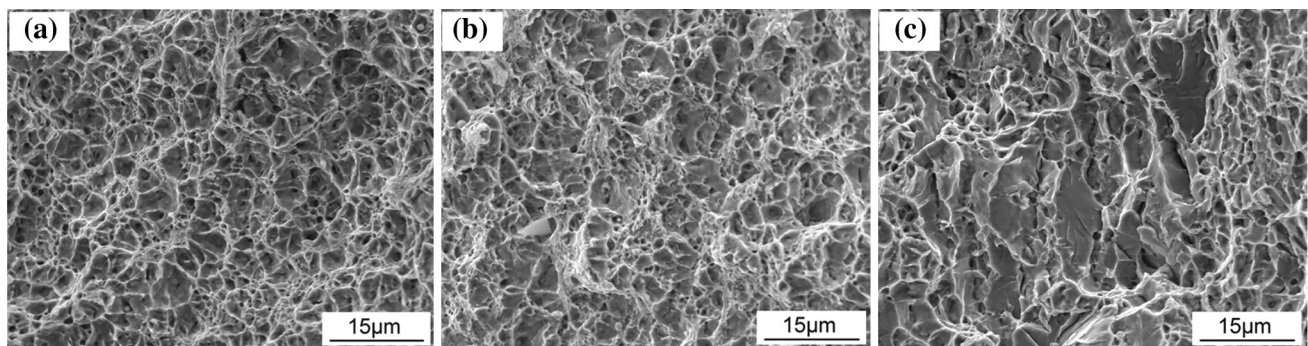


Fig. 7 SEM images on the fracture surfaces of IQ **a**, IA **b**, SQ **c**

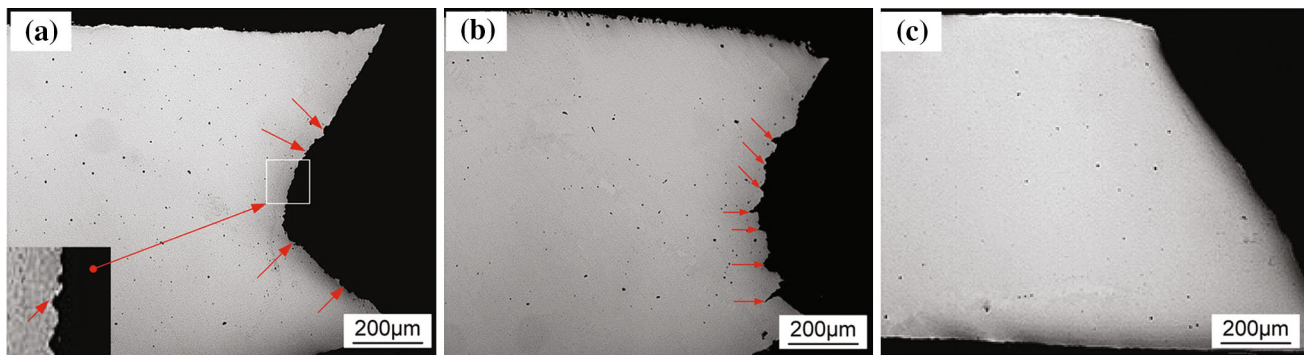


Fig. 8 Optical micrographs of the surfaces perpendicular to the fracture surface near the fracture surface: **a** IQ, **b** IA, **c** SQ

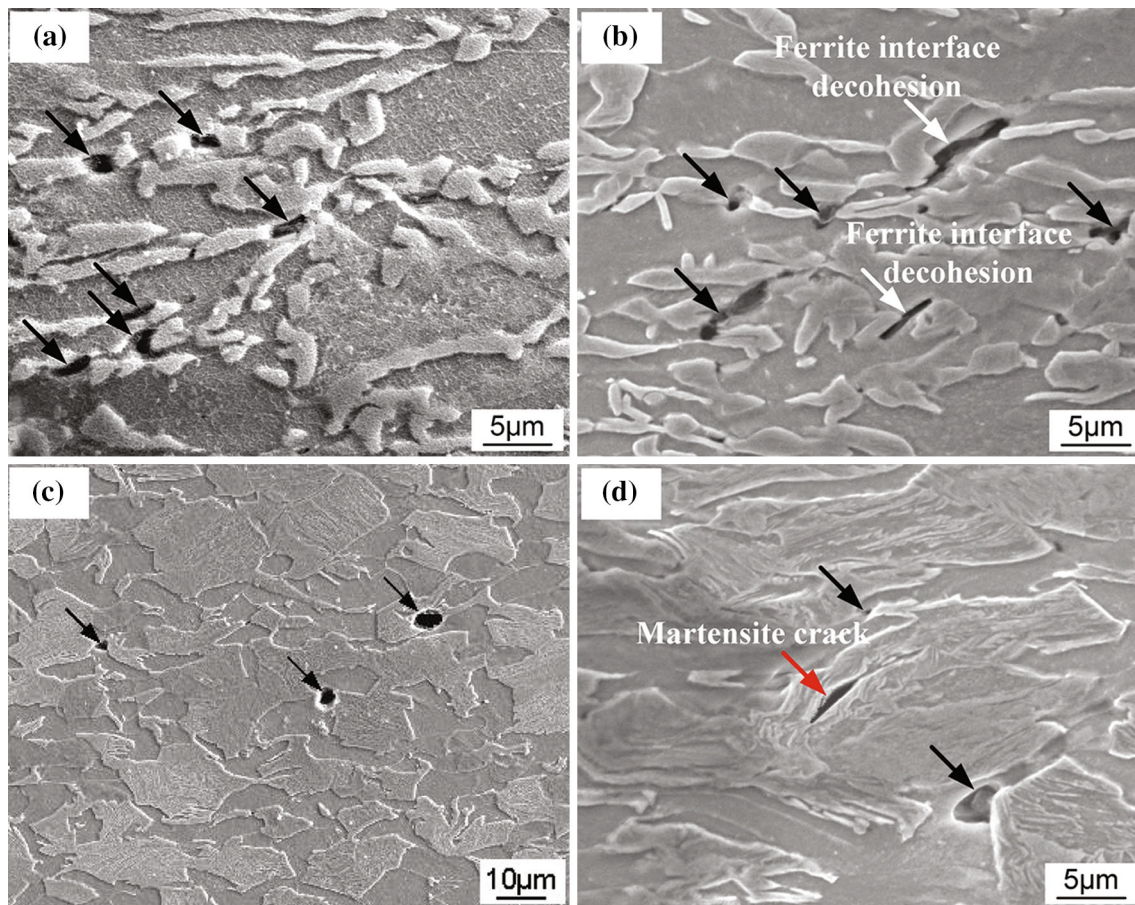


Fig. 9 SEM images of subsurfaces close to the fracture surface: **a** IQ, **b** IA, **c**, **d** SQ samples. The *arrows* indicate the sites of crack and/or void nucleation

However, martensite cracking is only present in SQ sample as marked by the red arrow in Fig. 9d. According to Uggowitzer and Stüwe [44], the fractured martensite acts as a sharp notch, leading to cleavage crack in the ferrite. As can be seen from Fig. 9b, the presence of microvoids within the ferrite grains for IA sample (as marked by the white arrow in Fig. 9b) allows one to infer that the ferrite phase is effectively restrained against plasticity by the

surrounding martensite in IA sample and this leads to higher stress concentration during ferrite/martensite interfaces. As a consequence, the microvoids formed at martensite/ferrite interfaces can easily grow along the interface and promote the void coalescence resulting into lower values of the elongation to failure. However, microvoids only form at the ferrite/martensite interfaces in IQ sample (Fig. 9a); in this case, fine and fibrous

martensite morphologies may restrict the growth of microvoids as they frequently encounter the discontinuities in the ferrite/martensite interfaces. In addition, lower stress concentration was expected due to uniform and fine distribution of the martensite in the IQ sample.

4 Conclusions

1. The microstructure of DP steels varied significantly with the heat-treatment schedule: IQ treatment produced fine and fibrous martensite uniformly distributed in the ferrite matrix; IA treatment showed a network martensite along the ferrite grain boundaries; SQ treatment showed that the martensite reveals coarse blocky microstructure;
2. Among all the specimens, IQ treatment provided the best combination of the strength and ductility, and highest magnitude of strain-hardening ability, and the strength–elongation (UTS \times UE) balance of IQ treated specimen was 9285 MPa%.
3. The variation in martensite volume fraction, size and morphology under different heat treatments was responsible for changing the fracture mechanism.
4. Analyses of tensile subsurfaces have revealed that ferrite–martensite interface decohesion was the predominant sites of the void nucleation. However, the microcracks were nucleated by the fracture of martensite in SQ sample, and microvoids were also nucleated within the ferrite grain in IA sample.

Acknowledgments This work was financially supported by the National Key Project of Scientific and Technical Supporting Programs of China (No. 2011CB606306-2) and the National Natural Science Foundation of China (Grant No. 51204048).

References

- [1] J. Kadkhodapour, A. Butz, S. Ziaei-Rad, *Acta Mater.* **59**, 2575 (2011)
- [2] A. Huseyin, K.Z. Havva, K. Ceylan, *J. Iron. Steel Res. Int.* **17**, 73 (2010)
- [3] J.J. Luo, W. Shi, Q.L. Huang, L. Li, *J. Iron. Steel Res. Int.* **17**, 54 (2010)
- [4] R.O. Rocha, T.M.F. Melo, E.V. Pereloma, D.B. Santos, *Mater. Sci. Eng., A* **391**, 296 (2005)
- [5] G.A. Cingara, Y. Ososkov, M.K. Jain, D.S. Wilkinson, *Mater. Sci. Eng., A* **516**, 7 (2009)
- [6] M. Asadi, B.C.D. Cooman, H. Palkowski, *Mater. Sci. Eng., A* **538**, 42 (2012)
- [7] H. Ghassemi-Armaki, R. Maab, S.P. Bhat, *Acta Mater.* **62**, 197 (2014)
- [8] Y. Sun, X.F. Li, X.Y. Yu, *Acta Metall. Sin. (Engl. Lett.)* **27**, 101 (2014)
- [9] M. Koyama, C.C. Tasan, E. Akiyama, K. Tsuzaki, D. Raabe, *Acta Mater.* **70**, 174 (2014)
- [10] X. Sun, K.S. Choi, W.N. Liu, M.A. Khaleel, *Int. J. Plast.* **25**, 1888 (2009)
- [11] J. Kadkhodapour, S. Schmauder, D. Raabe, S. Ziaei-Rad, U. Weber, M. Calcagnotto, *Acta Mater.* **59**, 4387 (2011)
- [12] C.C. Tasan, J.P.M. Hoefnagels, M.G.D. Geers, *Scr. Mater.* **63**, 316 (2010)
- [13] H. Ghadbeigi, C. Pinna, S. Celotto, J.R. Yates, *Mater. Sci. Eng., A* **527**, 5026 (2010)
- [14] N. Peranio, Y.J. Li, F. Roters, D. Raabe, *Mater. Sci. Eng., A* **527**, 4161 (2010)
- [15] A. Bag, K.K. Ray, E.S. Dwarakadasa, *Metall. Mater. Trans. A* **30**, 1193 (1999)
- [16] M.A. Maleque, Y.M. Poon, H.H. Masjuki, *J. Mater. Process. Technol.* **153–154**, 482 (2004)
- [17] D. Das, P.P. Chattopadhyay, *J. Mater. Sci.* **44**, 2957 (2009)
- [18] N.J. Kim, G. Thomas, *Metall. Trans. A* **12**, 483 (1981)
- [19] G. Speich, V. Demarest, R. Miller, *Metall. Mater. Trans. A* **12**, 1419 (1981)
- [20] M. Calcagnotto, Y. Adachi, D. Ponge, D. Raabe, *Acta Mater.* **59**, 658 (2011)
- [21] M. Calcagnotto, D. Ponge, D. Raabe, *Mater. Sci. Eng., A* **527**, 7832 (2010)
- [22] N. Saeidi, F. Ashrafizadeh, B. Niroumand, *Mater. Sci. Eng., A* **599**, 145 (2014)
- [23] Y. Mazaheri, A. Kermanpur, A. Najamizadeh, *ISIJ Int.* **55**, 218 (2015)
- [24] Y. Mazaheri, A. Kermanpur, A. Najafizadeh, *Mater. Sci. Eng., A* **619**, 1 (2014)
- [25] A.R. Marder, *Metall. Trans. A* **13**, 85 (1982)
- [26] K. Park, M. Nishiyama, N. Nakada, T. Tsuchiyama, *Mater. Sci. Eng., A* **604**, 135 (2014)
- [27] A. Karmakar, M. Ghosh, D. Chakrabarti, *Mater. Sci. Eng., A* **564**, 389 (2013)
- [28] T. Bhattacharyya, T. Sakaki, G.J. Weng, *Metall. Trans. A* **24**, 301 (1993)
- [29] A. Hüseyin, K.Z. Havva, K. Ceylan, *J. Iron. Steel Res. Int.* **17**, 73 (2010)
- [30] A. Bayram, A. Uguz, M. Ula, *Mater. Charact.* **43**, 259 (1999)
- [31] P. Li, J. Li, W.B. Hua, D.H. Xu, *J. Alloys Compd.* **578**, 320 (2013)
- [32] R.R. Mohanty, O.A. Girina, N.M. Fonstein, *Metall. Mater. Trans. A* **42**, 3680 (2011)
- [33] M. Türkmen, S. Gündüz, *Acta Metall. Sin. (Engl. Lett.)* **27**, 279 (2014)
- [34] H.F. Lan, X.H. Liu, L.X. Du, *Acta Metall. Sin. (Engl. Lett.)* **25**, 443 (2012)
- [35] K.T. Park, S.Y. Han, B.D. Ahn, D.H. Shin, Y.K. Lee, K.K. Um, *Scr. Mater.* **51**, 909 (2004)
- [36] M. Calcagnotto, D. Ponge, D. Raabe, *ISIJ Int.* **48**, 1096 (2008)
- [37] V. Colla, M. De Sanctis, A. Dimatteo, *Metall. Mater. Trans.* **40**, 2557 (2009)
- [38] W.J. Nie, C.J. Shang, H.L. Guan, X.B. Zhang, S.H. Chen, *Acta Metall. Sin.* **48**, 298 (2012). (in Chinese)
- [39] Y.I. Son, Y.K. Lee, K.T. Park, C.S. Lee, D.H. Shin, *Acta Mater.* **53**, 3125 (2005)
- [40] Y. Mazaheri, A. Kermanpur, A. Najafizadeh, N. Saeidi, *Mater. Sci. Eng., A* **612**, 54 (2014)
- [41] N.K. Balliger, T. Gladman, *Met. Sci.* **15**, 95 (1981)
- [42] M. Mazinani, W.J. Poole, *Metall. Mater. Trans. A* **38**, 328 (2007)
- [43] M. Sarwar, *J. Mater. Sci.* **31**, 2091 (1996)
- [44] P. Uggowitzer, H.P. Stüwe, *Mater. Sci. Eng.* **55**, 181 (1982)